Multiple magnetic transitions and electrical transport transformation of a $BaFeO_3$ cubic perovskite single crystal

Yuxuan Liu,[1,2] Zhehong Liu,[1,3] Zhi Li,[4] Shijun Qin,[1,3] Xubin Ye,[1,3] Xudong Shen,[1,3] Bowen Zhou,[1,3] Guanghui Zhou,[2,*] Stefano Agrestini,[5,6] Manuel Valvidares,[5] Hari Babu Vasili,[5] Zhiwei Hu,[6] and Youwen Long[1,3,7,†]

[1]*Beijing National Laboratory for Condensed Matter Physics, Institute of Physics, Chinese Academy of Sciences, Beijing 100190, China*

[2]*Department of Physics and Synergetic Innovation Center for Quantum Effects and Applications of Hunan, Hunan Normal University, Changsha 410081, China*

[3]*School of Physics, University of Chinese Academy of Sciences, Beijing 100049, China*

[4]*School of Materials Science and Engineering, Nanjing University of Science and Technology, 210094 Nanjing, China*

[5]*ALBA Synchrotron Light Source, E-08290 Cerdanyola del Vallès, Barcelona, Spain*

[6]*Max-Planck Institute for Chemical Physics of Solids, Nöthnitzer Straße 40, 01187 Dresden, Germany*

[7]*Songshan Lake Materials Laboratory, Dongguan, Guangdong 523808, China*

(Received 29 December 2019; revised manuscript received 6 March 2020; accepted 23 March 2020; published 15 April 2020)

Cubic perovskite $BaFeO_3$ single crystals with stoichiometric oxygen content were successfully grown by a two-step method. With decreasing temperature, the crystal experiences a spin-glassy transition at $T_{SG} \approx 181$ K, followed by a long-range spiral antiferromagnetic ordering at $T_N \approx 117$ K, and then a third spin transition at $T_N' \approx 97$ K, revealing the subtle magnetic competition and interactions. As a result, a smaller magnetic field (~0.4 T) can induce a metamagnetic transition towards a ferromagnetic state with the saturated magnetic moment about 3.2 μ_B/f.u. at 2 K. The easy magnetization axis looks to vary from the direction perpendicular to [111] to the [100] axis. Semiconducting behavior with a small activation energy is observed above T_N, whereas the spiral spin ordering changes the electrical transport to be likely half-metallic with considerable negative magnetoresistance effect.

DOI: 10.1103/PhysRevB.101.144421

I. INTRODUCTION

Iron-based oxides with unusually high Fe valence states such as Fe^{4+} show intriguing physical properties such as charge disproportionation, intermetallic charge transfer, metal-insulator transition, negative thermal expansion, etc. [1–6]. As the $AFe^{4+}O_3$ (A = Ca, Sr, Ba) perovskites are concerned [2,7,8], the orthorhombic $CaFeO_3$ experiences a charge-disproportionation transition around 290 K, accompanied by the reduction of crystal symmetry as well as the sharp variation in electrical transport. In magnetism, $CaFeO_3$ exhibits a spiral antiferromagnetic (AFM) ordering at the Néel temperature $T_N \approx 120$ K with the propagation vector $k//\langle 111\rangle$ direction [9,10]. Different from the distorted perovskite $CaFeO_3$, the analogous compound $SrFeO_3$ crystallizes into a simple cubic structure without FeO_6 octahedral distortion [11], since the electronic state of Fe in $SrFeO_3$ is dominated by $d^5\underline{L}$ configuration instead of d^4 configuration at the ground state with strong Jahn-Teller distortion [12]. Here the $\underline{L}$ stands for a ligand hole from the coordinated oxygen $2p$ states due to the considerable negative charge transfer energy $\Delta \approx -3$ eV (the energy needed to transfer an electron from ligand atom to transition metal) [4]. As a consequence, $SrFeO_3$ displays metallic conductivity [11]. In spite of the distinct structures and transport properties, $SrFeO_3$ shows similar spiral AFM ordering to that of $CaFeO_3$ with the propagation vector parallel to the $\langle 111\rangle$ direction, too [13]. By comparison, the spins between the adjacent layers rotate by about 46° in $SrFeO_3$ while they rotate by 60° in $CaFeO_3$ [10].

In contrast to the corner-sharing perovskite structures of $CaFeO_3$ and $SrFeO_3$, the large ionic size of Ba^{2+} causes $BaFeO_3$ to be a $6H$ or $12H$ hexagonal structure by sharing corners and edges of FeO_6 octahedra [14,15]. The cubic perovskite phase of $BaFeO_3$ was absent until 2011, when a topochemical method was adopted at a low synthesis reaction temperature (473 K) by using ozone as an oxidant [8]. Although the cubic $BaFeO_3$ also has a spiral AFM ground state, it shows lower magnetic field-induced ferromagnetic (FM) polarization, making this phase unique in all the iron-based compounds composed of an unusually high Fe^{4+} valence state. Unfortunately, however, the topochemically oxidizing method can only obtain a small amount of polycrystalline powders with the depth of about 1 μm, which severely restricts the study of bulk properties such as specific heat and electrical transport. Although lots of efforts were made to prepare cubic $BaFeO_3$ thin films [16–18], the magnetic ground state has always been changed into an FM state instead of the spiral AFM ground state as observed in powders, reflecting the sensitive effects of residual strain, reduced dimensionality,

*ghzhou@hunnu.edu.cn
†ywlong@iphy.ac.cn

and/or slight oxygen deficiency on the intrinsic physical properties of $BaFeO_3$. Consequently, the thin films show electrical insulating behavior with an energy band gap as large as 1.8 eV [18]. Such a large band gap looks incompatible with a high Fe^{4+} state possessing remarkable negative *p-d* charge transfer energy. To get deeper insight into the intrinsic physics of the cubic $BaFeO_3$ perovskite, it is pressingly needed to grow high-quality single crystals with stoichiometric oxygen content. In this paper, we prepare such single crystals by a two-step method combining a floating zone method with a high-pressure treatment technique [19]. Multiple magnetic transitions and spin-induced electrical transport variation are found to occur.

II. EXPERIMENTAL AND CALCULATION METHODS

The polycrystalline $BaFeO_{2.5}$ precursor was synthesized by a solid-state reaction method as reported elsewhere [20]. Then, the $BaFeO_{2.5}$ single crystal with a brownmillerite-type structure was grown by using a floating zone method in Ar atmosphere. The growth rate was $2\,\mathrm{mm\,h^{-1}}$. Finally, the brownmillerite-type $BaFeO_{2.5}$ precursor single crystal was treated on a cubic-anvil-type high-pressure apparatus at 5 GPa and 1000 K for 30 min with the usage of a $KClO_4$ oxidizing agent [21]. To identify the sample quality and determine the crystal orientation, powder x-ray diffraction (XRD) and Laue back reflection were measured at room temperature on a Huber diffractometer. Structural refinement was performed based on the Rietveld method using the GSAS package [22]. The thermogravimetric (TG) analysis was carried out using a Setaram TG-DTA system. The sample was heated up to 950 K in Ar flow with a heating speed of 10 K/min. The residual product was checked by XRD. Temperature dependence of dc magnetic susceptibility and isothermal magnetization were measured using a superconducting quantum interference device magnetometer (Quantum Design, MPMS-VSM). The ac magnetization, specific heat, and electrical transport properties were measured on a physical property measurement system (Quantum Design, PPMS-7T). X-ray magnetic circular-dichroism (XMCD) spectroscopic studies at the Fe-$L_{2,3}$ edges were performed applying a 6-T magnetic field at the BL29 BOREAS beamline at the ALBA Synchrotron Light Facility.

The band structures of $BaFeO_3$ with FM and G-type AFM states were calculated by a first-principles method based on density functional theory implemented in VASP with general gradient approximation plus Hubbard $U_{\mathrm{eff}} = 3.0\,\mathrm{eV}$ [23–25]. The projector augmented wave pseudopotentials with 600 eV energy cutoff was used in our calculation. For band dispersions, a $24 \times 24 \times 24$ k-point grid was adopted for their self-consistent calculations.

III. RESULTS AND DISCUSSION

Figure 1(a) shows the as-made $BaFeO_{2.5}$ and $BaFeO_3$ single crystals with black color. After high-pressure treatment, the $BaFeO_3$ crystals ~3 mm in diameter and height can be obtained. To determine the crystal structure, the single crystal was crushed into powders for XRD measurement. As shown in Fig. 1(b), the XRD pattern of $BaFeO_3$ can be well fitted on the basis of a simple cubic perovskite structure with space group $Pm\text{-}3m$. The refined lattice constant is $a = 3.968\,33(2)$ Å, which is slightly less than that reported on previous polycrystalline (3.971 06 Å) and thin film (~3.97 Å) samples [8,18], suggesting that the oxygen content in the current single crystal is closer to the stoichiometric value. To identify the single crystal quality, Laue back reflection was carried out. The sharp Laue diffraction spots indicate the successful growth of high-quality single crystal. As an example, the Laue spots for a high symmetrical plane of (100) and the related XRD pattern of this plane are shown in Fig. 1(c). Since the oxygen content plays a crucial role in the physical properties of $BaFeO_3$ [26,27], we performed TG measurement. As shown in Fig. 1(d), the oxygen starts to release on heating to about 370 K, and the mass is almost invariable above ~850 K. According to the mass loss as well as the final product ($BaFeO_{2.5}$), the oxygen content is determined to be 2.99 ± 0.02, suggesting the stoichiometric chemical composition and the formation of Fe^{4+} state in $BaFeO_3$ single crystal.

Figures 2(a)–2(c) show temperature dependence of dc magnetic susceptibility (χ), ac magnetization (M'), and specific heat (C_p) measured on $BaFeO_3$ single crystals, respectively. The zero-field-cooling (ZFC) and field-cooling (FC) modes were used for χ measurement by applying a magnetic field $H = 100\,\mathrm{Oe}$ parallel to the (110) and (111) planes. Different from the polycrystalline sample where only a single AFM transition is observed around 111 K [8], three magnetic transitions are found to occur in single crystal. With decreasing temperature, the χ experiences an anomaly around $T_{SG} \approx 181\,\mathrm{K}$, at which a frequency-dependent peak is observed in M' but there is no anomaly in C_p, indicating a spin-glassy transition. This can be understood on the basis of the spiral AFM ground state of $BaFeO_3$ [8], where the nearest-neighbor FM and next nearest-neighbor AFM competition is responsible for the spin-glass behavior [28,29]. On further cooling to $T_N \approx 117\,\mathrm{K}$, the ZFC and FC curves start to separate from each other. Based on powder neutron diffraction, a noncollinear spiral AFM spin structure was determined for the cubic perovskite phase of $BaFeO_3$ below about 111 K [8]. In this spiral spin structure, the propagation vector is along the [100] direction and the rotation angle is about 22°. Since the spins tend to orientate along the applied magnetic field during the susceptibility measurement, the separation between ZFC and FC curves occurring at the onset of $T_N \approx 117\,\mathrm{K}$ may suggest the formation of a long-range spiral AFM ordering [30,31]. Moreover, the C_p shows an apparent anomaly and the electrical transport behavior changes essentially (shown later) at T_N, providing convincing evidence for the presence of long-rang AFM phase transition, in agreement with the observation of a spiral AFM ordering in a polycrystalline sample near 111 K [8]. Furthermore, as the temperature decreases to $T_N' \approx 97\,\mathrm{K}$, both ZFC and FC curves exhibit a kink accompanied by the frequency-independent peak in M'. Besides, a remarkable separation is found to occur between the (110) and (111) planes at this temperature [see Fig. 2(a)]. These features may demonstrate a second AFM phase transition taking place in $BaFeO_3$ single crystal, although it cannot be distinguished in the polycrystalline sample. A possible origin for this transition may be attributed to spin reorientation. Alternatively, in the analogous cubic perovskite $SrFeO_3$, multiple AFM transitions

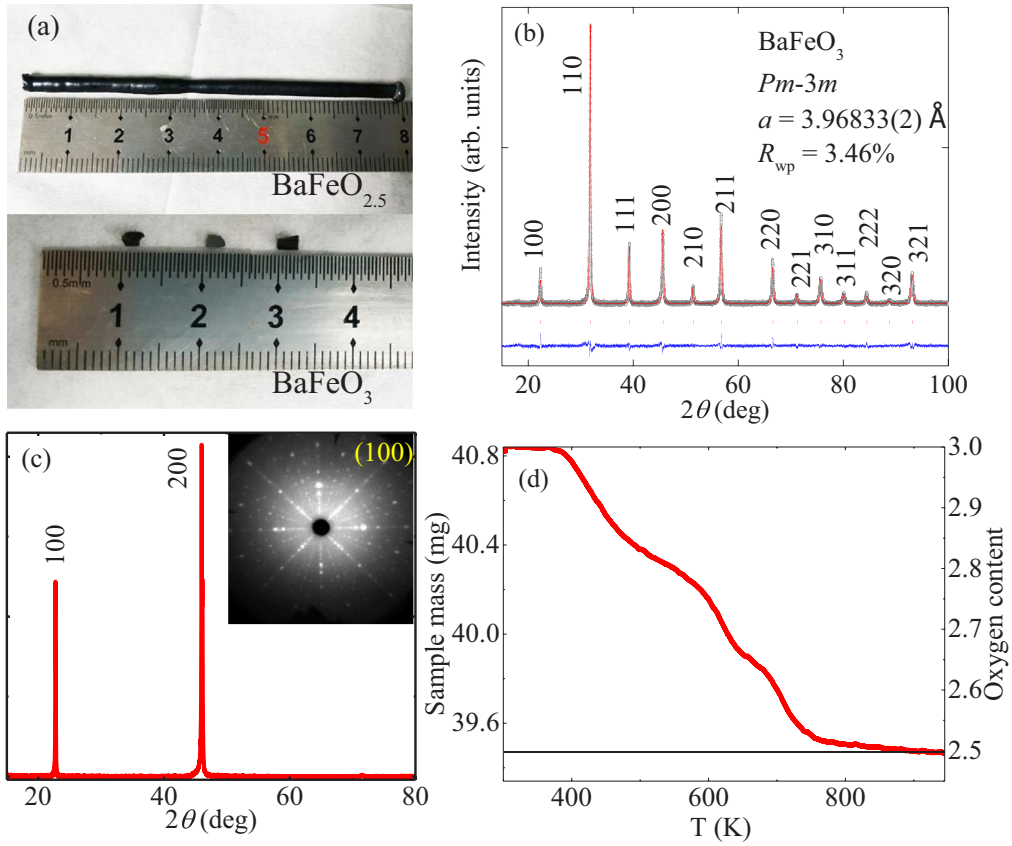

FIG. 1. (a) Morphology of $BaFeO_{2.5}$ and $BaFeO_3$ single crystals. (b) Powder XRD pattern and Rietveld refinement results of pulverized $BaFeO_3$ crystal measured at room temperature. The observed (black circles), calculated (red line), and difference (blue line) patterns are shown. The ticks indicate the allowed Bragg reflections with space group *Pm*-3*m*. (c) XRD pattern for the high symmetrical (100) plane. The inset shows the Laue diffraction spots of this plane. (d) Temperature dependence of sample mass (left *y* axis) and oxygen content (right *y* axis) derived from the TG measurement.

are also observed in its single crystal due to the variation of spiral AFM propagation vectors [32]. Similar change probably occurs in the current $BaFeO_3$ single crystal at T_N'. The inset of Fig. 2(a) shows the Curie-Weiss fitting for the inverse χ above 210 K, yielding a Weiss temperature $\theta = 165.5(6)$ K and a Curie constant $C = 4.73(1)$ K emu mol^{-1}. The positive θ implies the occurrence of nearest-neighbor FM interactions as expected from the spiral magnetic structure composed of rotated FM planes, although the whole spin structure is AFM. According to the Curie constant, the effective magnetic moment is calculated to be $\mu_{\text{eff}} = 6.15(1)\mu_B$/f.u. In comparison, this value is closer to the spin-only theoretical value for a high-spin Fe^{3+} ion (5.92 μ_B/f.u.) than that of an Fe^{4+} ion (4.90 μ_B/f.u.), suggesting that the electronic state of Fe in $BaFeO_3$ can be mainly regarded as $3d^5\underline{L}$. It means that there is a considerable negative charge transfer energy in $BaFeO_3$ [33,34]. At low temperature (<12 K), the specific heat data can be fitted by the function $C_p = \gamma T + \beta T^3$ [see Fig. 2(c)], producing $\gamma = 2.78(4) \times 10^{-2}$ J mol^{-1} K^{-2} and $\beta = 8.4(3) \times 10^{-5}$ J mol^{-1} K^{-4}. The significant Sommerfeld coefficient is indicative of an itinerant electronic feature, in accordance with the dominated $3d^5\underline{L}$ state possessing strong *d*-*p* hybridization.

The isothermal magnetization curves measured at selected temperatures with $H//(100)$ are shown in Fig. 3(a), where the magnetic field is set at 5 T and scans from 5 to −5, and then to 5 T. At the first glance, $BaFeO_3$ shows soft FM behavior with the saturated magnetic moment up to 3.2 μ_B/f.u. at 5 T and 2 K. The detected saturation moment is somewhat smaller than the magnetic moment of a high-spin Fe^{4+} or an $Fe^{3+}\underline{L}$ state in the assumption of a local electronic model, suggesting that some electrons contribute to electrical itinerancy. In analogy with the FM metal $SrCoO_3$ with localized t_{2g} and itinerant e_g electrons [35], the t_{2g} electrons of Fe ions in $BaFeO_3$ should contribute to the localized spin moment, while the e_g electrons mainly take part in electrical transport. On the other hand, Fig. 3(b) shows the field-dependent magnetization with increasing field from 0 to 5 T (the data above 2 T are not shown). Consistent with the AFM ground state, the magnetization of $BaFeO_3$ almost shows a linear relationship with fields below about 0.3 T. However, a smaller field about 0.4 T can trigger a metamagnetic transition from the initial AFM to a FM state as represented in Fig. 3(a). If one compares the magnetization curves above 0.5 T with the field along different planes shown in Fig. 3(b), during the field increasing process, the curves with $H//(111)$ and (100) cross with each other around 0.7 T, and both curves exhibit larger magnetic moments than that with $H//(110)$ when the magnetic moment does not become saturated below about 1.5 T. These features may indicate the easy magnetization axis changes from the

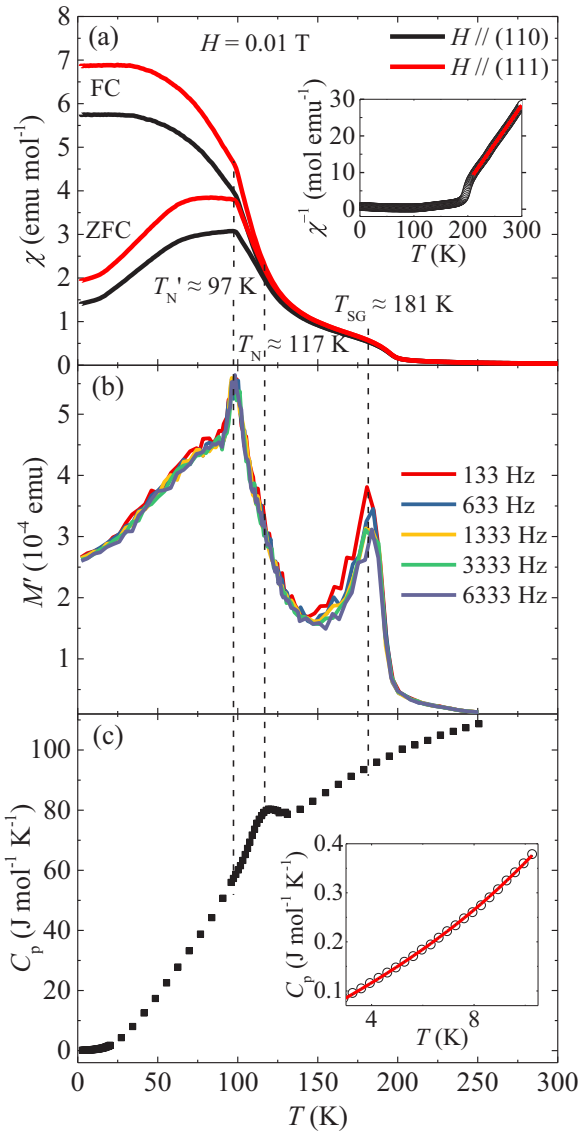

FIG. 2. Temperature dependence of (a) dc magnetic susceptibility with field parallel to (110) and (111) planes, (b) ac magnetic susceptibility measured at different frequencies, and (c) specific heat for $BaFeO_3$. The inset of (a) shows the inverse susceptibility and the Curie-Weiss law fitting (red line) for the (110) plane between 210 and 300 K. The inset of (c) shows the fitting result (red curve) for specific heat below 12 K as described in the text.

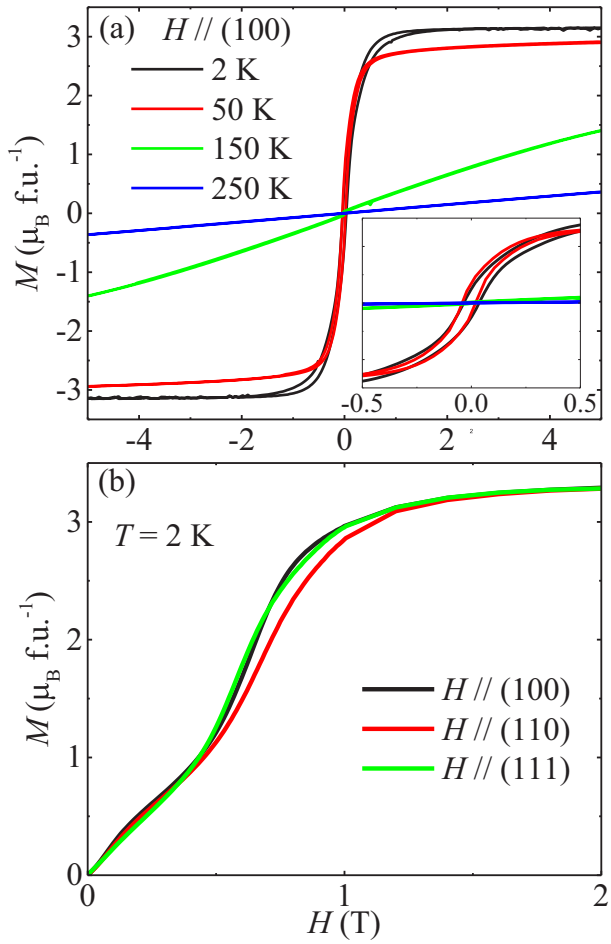

FIG. 3. Field dependence of (a) isothermal magnetization curves measured at selected temperatures with field parallel to the (100) plane, and (b) magnetization measured at 2 K for different planes of $BaFeO_3$. The magnetic field in (a) is set at 5 T and scans from 5 to −5 and then to 5 T, and in (b) from 0 to 5 T (the data above 2 T are not shown). The inset of (a) shows an enlarged view for the lower field behavior.

direction perpendicular to [111] to the [100] axis with increasing field to 0.7 T. It means that the spin orientation of $BaFeO_3$ is sensitive to external conditions. The third magnetic transition occurring at $T_N' \approx 97$ K is thus probably attributed to a spin reorientation (or propagation vector variation as mentioned above), but the detailed mechanism remains to be studied in the future. As shown in the inset of Fig. 3(a), once the field-induced metamagnetic transition completes with applied field up to 5 T, during the field decreasing process, magnetic hysteresis behavior can be found to occur below T_N (e.g., at 2 and 50 K) with a small coercive field about 400 Oe.

To further analyze the spin magnetic moment (M_{spin}) and orbital magnetic moment (M_{orb}), the XMCD was measured at Fe-$L_{2,3}$ edges under a 6-T field, as shown in Figs. 4(a) and 4(b). The XMCD curve $\Delta\mu$ is the difference between the x-ray absorption spectroscopy (XAS) with photon spin parallel (μ^+) and antiparallel (μ^-) to the applied magnetic field. The XAS and XMCD curves of $BaFeO_3$ single crystal are rather broad revealing a strong covalent property of the high Fe^{4+} state [35,36]. In comparison, the size of the XMCD signal at the Fe-L_3 edge in our $BaFeO_3$ single crystal reaches to 24%, which is larger than that detected in the thin film (∼18%) [36] and the polycrystalline powder sample (10%) [37]. Furthermore, according to the XMCD sum rules [38,39], the M_{spin} and M_{orb} of $BaFeO_3$ crystal are calculated to be about 1.537 and 0.046 μ_B/f.u. at 2 K. The sum-rule analysis would underestimate the magnetization of Fe taking into account the strong overlapping between the Fe-L_3 and -L_2 edges owing to the considerable multiplet interactions and saturation effects in the total-electron-yield method [40,41]. By using the same correction coefficient as adopted for $BaFeO_3$ thin film [36], namely, 1/0.58 and 1/0.88 to compensate the reduced moment due to overlapping between the Fe-L_3 and Fe-L_2

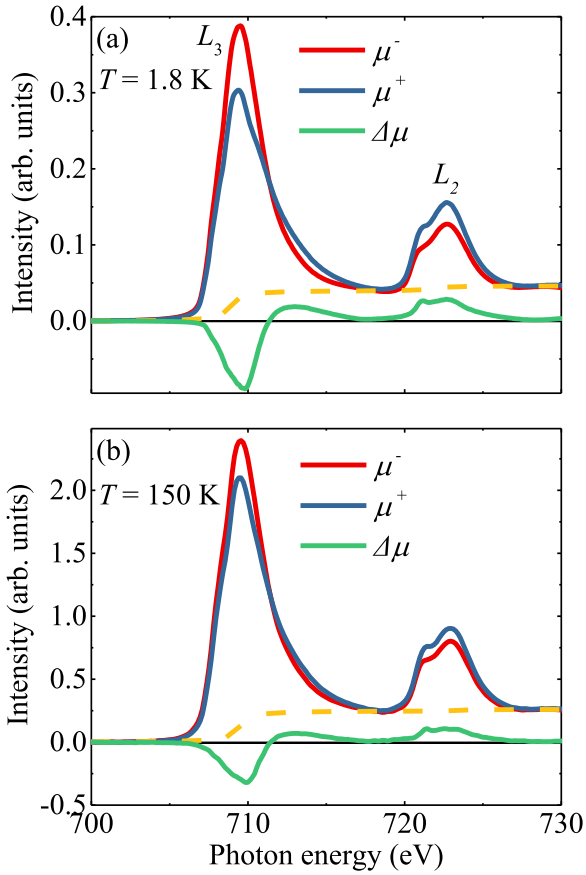

FIG. 4. XMCD spectra for Fe-$L_{2,3}$ edges measured at (a) 2 K and (b) 150 K for $BaFeO_3$. The photon spin is aligned parallel (μ^+ blue line) and antiparallel (μ^- red line) to the applied magnetic field. The XMCD signals $\Delta\mu = \mu^+ - \mu^-$ are shown in green line. The dotted line stands for the contribution of the background.

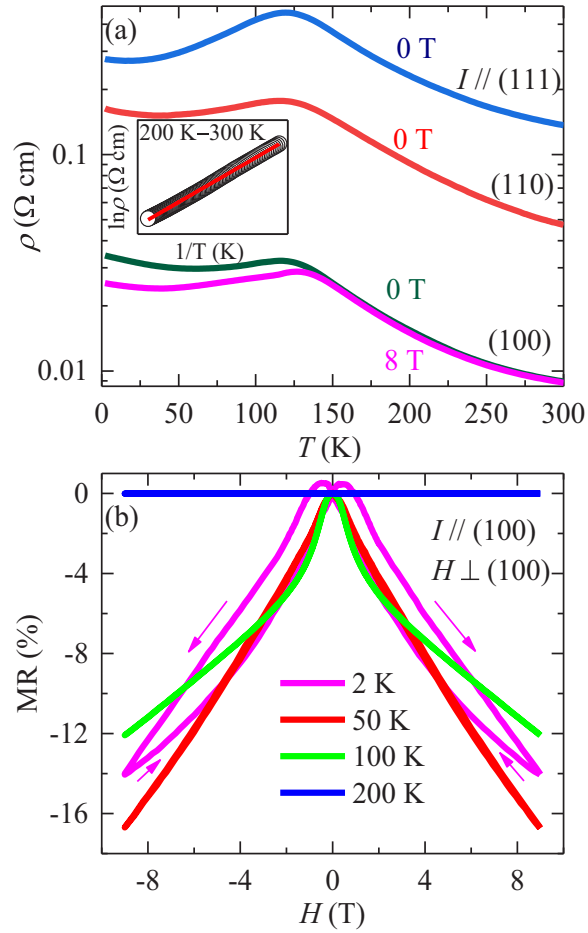

FIG. 5. (a) Temperature dependence of resistivity measured for different planes of $BaFeO_3$. The inset shows the fitting result (red line) using the thermal excitation model for the (111) plane. (b) Field dependence of magnetoresistance effects measured at different temperatures.

edges and the saturation effects in total-electron-yield mode, respectively [36,42], we obtained the $M_{spin} \approx 3.01\,\mu_B$/f.u. and $M_{orb} \approx 0.095\,\mu_B$/f.u. at 2 K. Therefore, the total magnetic moment is about $3.11\,\mu_B$/f.u., which is close to the saturated magnetic moment measured in magnetization at the same temperature [see Fig. 3(a)]. Obviously, the orbital contribution to the total moment is negligible in $BaFeO_3$ as expected for half-fully occupied t_{2g}/e_g orbitals in a dominant $3d^5\underline{L}$ ground state. The XMCD measured at 6 T and 150 K is shown in Fig. 4(b). The $\Delta\mu$ is suppressed compared with that measured at 2 K [Fig. 4(a)]. By using the same calculation as mentioned above, we obtained the $M_{spin} \approx 1.75$, $M_{orb} \approx 0.074$, and $M_{total} \approx 1.82\,\mu_B$/f.u., which is also comparable with the magnetization measurement result.

Figure 5(a) shows the temperature-dependent resistivity of $BaFeO_3$ single crystal with electric current I//(100), (110), and (111) planes. Although the absolute values of resistivity change somewhat in these planes, they exhibit very similar temperature dependence. Specifically, as the temperature decreases, the resistivity smoothly increases and experiences a kink at T_N, followed by a slight decrease with a small upturn at lower temperatures. It means that a semiconductor to metal-like transition takes place at T_N due to the long-range spiral AFM ordering. Using the (111) plane as an example, above 200 K, the resistivity can be well fitted by a thermal activation model as shown in the inset of Fig. 5(a), producing the activation energy $E = 27.6$ meV. This is essentially different from the strong insulating behavior observed in thin films [18,43], where a considerable optical gap as large as 1.8 eV is reported [18]. For the (100) plane, the resistivity was measured at both 0 and 8 T. Apparently, the magnetic field can decrease the electrical resistivity below T_N. We thus at selected temperatures performed a field scan for resistivity with the I//(100) but $H \perp$(100) plane. The magnetoresistance (MR) effects were calculated using the function $MR(\%) = 100\% \times [\rho(H) - \rho(0)]/\rho(0)$. As shown in Fig. 5(b), at 2 K, the resistivity slightly increases with field up to about 0.4 T, and then sharply decreases with increasing field. It means that the AFM ground state has a small positive MR effect, whereas the sign changes to be negative once the field-induced FM state emerges. At 50 and 100 K, the positive MR behavior is not discernible, probably due to the thermal perturbation on the subtle spiral AFM ground state. The absolute MR value observed at 9 T and 2 K is 14.1%, while it increases to 16.8% at the same field and 50 K. Above T_{SG}, e.g., at 200 K, the MR effect becomes negligible.

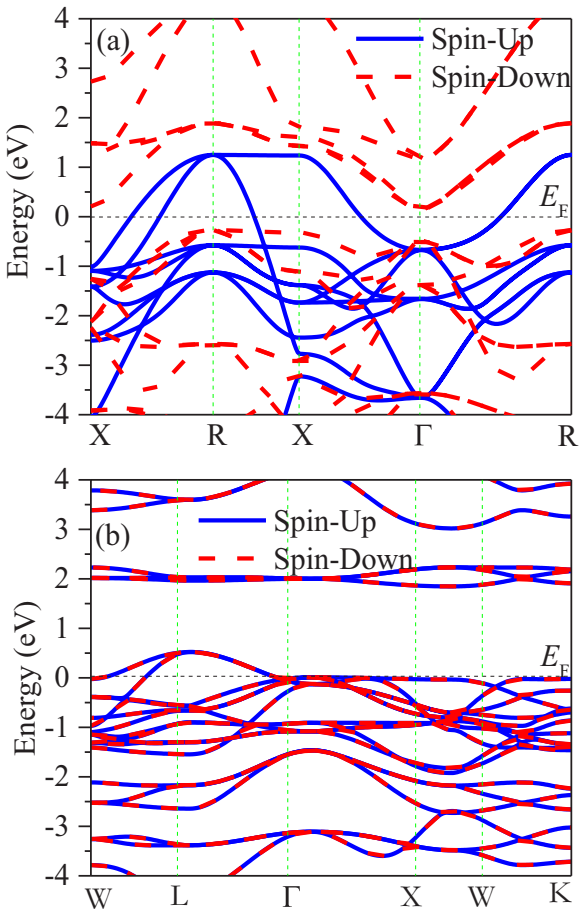

FIG. 6. First-principles calculations results for the electronic density of state of $BaFeO_3$ near the Fermi level (E_F) with (a) FM and (b) G-type AFM spin configurations.

To get deeper insight into the electronic properties, first-principles calculations were carried out. For simplification, we only consider the FM and G-type AFM spin configurations. Figures 6(a) and 6(b) show the electronic density of states near the Fermi level for these two types of spin configuration. In the FM configuration, the spin-up channel crosses the Fermi surface and contributes to electrical transport, whereas the spin-down channel opens a moderate energy gap about 0.5 eV, suggesting half-metallic behavior. In contrast, the G-type AFM spin leads to metallic energy band structure. In experiment, $BaFeO_3$ has a spiral AFM structure with the propagation vector along the ⟨100⟩ direction [8]. Since the rotation angle between the adjacent FM layers is only about 22°, this kind of spin structure is close to a collinear FM. Therefore, $BaFeO_3$ probably exhibits half-metal-like electrical transport property below T_N.

IV. CONCLUSION

In summary, we grew $BaFeO_3$ cubic perovskite single crystals using a floating zone method combined with a high-pressure treatment technique. The TG analysis confirms the stoichiometric oxygen content. Although only a single magnetic transition is observed in the polycrystalline sample, the current single crystal shows three magnetic transitions, i.e., a spin-glassy transition at about 181 K, a long-range spiral AFM ordering at ∼117 K, and a third transition around 97 K. The AFM ground state of $BaFeO_3$ is very sensitive to magnetic field, so that a moderate field can induce a metamagnetic transition to an FM state with the saturated magnetic moment about 3.2 μ_B/f.u. Compared with the spin moment, the orbital moment is negligible as confirmed by XMCD analysis. Semiconducting behavior is found to occur in $BaFeO_3$ in the paramagnetic region. However, the long-range spiral AFM ordering changes the electrical transport to be possibly half-metallic with a spin-up conducting channel and a spin-down insulating channel with remarkable negative MR effects below T_N.

ACKNOWLEDGMENTS

This work was supported by the National Key R&D Program of China (Grants No. 2018YFE0103200 and No. 2018YFA0305700), the National Natural Science Foundation of China (Grants No. 51772324, No. 11934017, No. 11921004, and No. 11574378), and the Chinese Academy of Sciences (Grants No. QYZDB–SSW–SLH013 and No. GJHZ1773).

[1] P. M. Woodward, D. E. Cox, E. Moshopoulou, A. W. Sleight, and S. Morimoto, Phys. Rev. B **62**, 844 (2000).
[2] C. X. Zhang, H. L. Xia, H. Liu, Y. M. Dai, B. Xu, R. Yang, Z. Y. Qiu, Q. T. Sui, Y. W. Long, S. Meng, and X. G. Qiu, Phys. Rev. B **95**, 064104 (2017).
[3] T. Kawakami, S. Nasu, T. Sasaki, K. Kuzushita, S. Morimoto, S. Endo, T. Yamada, S. Kawasaki, and M. Takano, Phys. Rev. Lett. **88**, 037602 (2002).
[4] A. E. Bocquet, A. Fujimori, T. Mizokawa, T. Saitoh, H. Namatame, S. Suga, N. Kimizuka, Y. Takeda, and M. Takano, Phys. Rev. B **45**, 1561 (1992).
[5] I. Yamada, K. Tsuchida, K. Ohgushi, N. Hayashi, J. Kim, N. Tsuji, R. Takahashi, M. Matsushita, N. Nishiyama, T. Inoue, T. Irifune, K. Kato, M. Takata, and M. Takano, Angew. Chem., Int. Ed. **50**, 6579 (2011).
[6] N. Hayashi, T. Terashima, and M. Takano, J. Mater. Chem. **11**, 2235 (2001).
[7] T. Takeda, Y. Yamaguchi, and H. Watanabe, J. Phys. Soc. Jpn. **33**, 967 (1972).
[8] N. Hayashi, T. Yamamoto, H. Kageyama, M. Nishi, Y. Watanabe, T. Kawakami, Y. Matsushita, A. Fujimori, and M. Takano, Angew. Chem., Int. Ed. **50**, 12547 (2011).
[9] S. Kawasaki, M. Takano, R. Kanno, T. Takeda, and A. Fujimori, J. Phys. Soc. Jpn. **67**, 1529 (1998).
[10] T. Takeda, R. Kanno, Y. Kawamoto, M. Takano, S. Kawasaki, T. Kamiyama, and F. Izumi, Solid State Sci. **2**, 673 (2000).

[11] P. Adler, A. Lebon, V. Damljanović, C. Ulrich, C. Bernhard, A. V. Boris, A. Maljuk, C. T. Lin, and B. Keimer, Phys. Rev. B **73**, 094451 (2006).
[12] I. Solovyev, N. Hamada, and K. Terakura, Phys. Rev. Lett. **76**, 4825 (1996).
[13] H. Oda, Y. Yamaguchi, H. Takei, and H. Watanabe, J. Phys. Soc. Jpn. **42**, 101 (1977).
[14] K. Mori, T. Kamiyama, H. Kobayashi, T. Otomo, K. Nishiyama, M. Sugiyama, K. Itoh, T. Fukunaga, and S. Ikeda, J. Appl. Crystallogr. **40**, s501 (2007).
[15] Y. Takeda, M. Shimada, F. Kanamaru, M. Koizumi, and N. Yamamoto, Mater. Res. Bull. **9**, 537 (1974).
[16] T. Matsui, H. Tanaka, N. Fujimura, T. Ito, H. Mabuchi, and K. Morii, Appl. Phys. Lett. **81**, 2764 (2002).
[17] C. Callender, D. P. Norton, R. Das, A. F. Hebard, and J. D. Budai, Appl. Phys. Lett. **92**, 012514 (2008).
[18] S. Chakraverty, T. Matsuda, N. Ogawa, H. Wadati, E. Ikenaga, M. Kawasaki, Y. Tokura, and H. Y. Hwang, Appl. Phys. Lett. **103**, 142416 (2013).
[19] H. Sakai, J. Fujioka, T. Fukuda, D. Okuyama, D. Hashizume, F. Kagawa, H. Nakao, Y. Murakami, T. Arima, A. Q. R. Baron, Y. Taguchi, and Y. Tokura, Phys. Rev. Lett. **107**, 137601 (2011).
[20] O. Clemens, M. Gröting, R. Witte, J. M. Perez-Mato, C. Loho, F. J. Berry, R. Kruk, K. S. Knight, A. J. Wright, H. Hahn, and P. R. Slater, Inorg. Chem. **53**, 5911 (2014).
[21] Y. W. Long, Y. Kaneko, S. Ishiwata, Y. Tokunaga, T. Matsuda, H. Wadati, Y. Tanaka, S. Shin, Y. Tokura, and Y. Taguchi, Phys. Rev. B **86**, 064436 (2012).
[22] B. Toby, J. Appl. Crystallogr. **34**, 210 (2001).
[23] G. Kresse and J. Hafner, Phys. Rev. B **47**, 558 (1993).
[24] G. Kresse and J. Furthmüller, Phys. Rev. B **54**, 11169 (1996).
[25] S. L. Dudarev, G. A. Botton, S. Y. Savrasov, C. J. Humphreys, and A. P. Sutton, Phys. Rev. B **57**, 1505 (1998).
[26] B. Ribeiro, R. P. Borges, R. C. da Silva, N. Franco, P. Ferreira, E. Alves, B. Berini, A. Fouchet, N. Keller, and M. Godinho, J. Appl. Phys. **111**, 113923 (2012).
[27] I. Gil de Muro, M. Insausti, L. Lezama, and T. Rojo, J. Solid State Chem. **178**, 1712 (2005).
[28] X. Ye, Z. Liu, W. Wang, Z. Hu, H.-J. Lin, S.-C. Weng, C.-T. Chen, R. Yu, L.-H. Tjeng, and Y. Long, J. Phys.: Condens. Matter **32**, 075701 (2019).
[29] J. Guo, X. Ye, Z. Liu, W. Wang, S. Qin, B. Zhou, Z. Hu, H.-J. Lin, C.-T. Chen, R. Yu, L. H. Tjeng, and Y. Long, J. Solid State Chem. **278**, 120921 (2019).
[30] T. Krenke, M. Acet, E. F. Wassermann, X. Moya, L. Mañosa, and A. Planes, Phys. Rev. B **72**, 014412 (2005).
[31] D. N. H. Nam, K. Jonason, P. Nordblad, N. V. Khiem, and N. X. Phuc, Phys. Rev. B **59**, 4189 (1999).
[32] S. Ishiwata, T. Nakajima, J.-H. Kim, D. S. Inosov, N. Kanazawa, J. S. White, J. L. Gavilano, R. Georgii, K. M. Seemann, G. Brandl, P. Manuel, D. D. Khalyavin, S. Seki, Y. Tokunaga, M. Kinoshita, Y. W. Long, Y. Kaneko, Y. Taguchi, T. Arima, and B. Keimer *et al.*, Phys. Rev. B **101**, 134406 (2020).
[33] J. Zaanen, G. A. Sawatzky, and J. W. Allen, Phys. Rev. Lett. **55**, 418 (1985).
[34] Z. Li, R. Laskowski, T. Iitaka, and T. Tohyama, Phys. Rev. B **85**, 134419 (2012).
[35] Y. Long, Y. Kaneko, S. Ishiwata, Y. Taguchi, and Y. Tokura, J. Phys.: Condens. Matter **23**, 245601 (2011).
[36] T. Tsuyama, T. Matsuda, S. Chakraverty, J. Okamoto, E. Ikenaga, A. Tanaka, T. Mizokawa, H. Y. Hwang, Y. Tokura, and H. Wadati, Phys. Rev. B **91**, 115101 (2015).
[37] M. Mizumaki, K. Yoshii, N. Hayashi, T. Saito, Y. Shimakawa, and M. Takano, J. Appl. Phys. **114**, 073901 (2013).
[38] B. T. Thole, P. Carra, F. Sette, and G. van der Laan, Phys. Rev. Lett. **68**, 1943 (1992).
[39] P. Carra, B. T. Thole, M. Altarelli, and X. Wang, Phys. Rev. Lett. **70**, 694 (1993).
[40] Y. Teramura, A. Tanaka, and T. Jo, J. Phys. Soc. Jpn. **65**, 1053 (1996).
[41] T. Koide, H. Miyauchi, J. Okamoto, T. Shidara, T. Sekine, T. Saitoh, A. Fujimori, H. Fukutani, M. Takano, and Y. Takeda, Phys. Rev. Lett. **87**, 246404 (2001).
[42] R. Nakajima, J. Stöhr, and Y. U. Idzerda, Phys. Rev. B **59**, 6421 (1999).
[43] T. Matsui, E. Taketani, N. Fujimura, T. Ito, and K. Morii, J. Appl. Phys. **93**, 6993 (2003).